Distinct structural mechanisms drive gain-of-function activation of TMEM16E in gnathodiaphyseal dysplasia

Eleonora Di Zanni[1], Omar E. Alvarenga[1,2], Nicole Rychlik[1,3,4$], Zhang Feng[1#], Elizabeth D. Kim[1], George Khelashvili[5], Alessio Accardi[1,6*]

1 Department of Anesthesiology, Weill Cornell Medicine; 2 Physiology, Biophysics, and Systems Biology Graduate Program, Weill Cornell Medicine; 3 ChemBion graduate program, University of Münster, Münster, Germany; 4 Institute of Physiology I, University of Münster, Münster, Germany; 5 Department of Computational and Systems Biomedicine, Weill Cornell Medicine; 6 Department of Biochemistry and Biophysics, Weill Cornell Medicine.

$ Nicole Rychlik present address: Institute of Physiology I, University of Münster, Münster, Germany; Department of Neurology, University Hospital Münster, Münster, Germany

Zhang Feng present address: School of Life Sciences, Nanjing Medical University, Changzhou, China

* correspondence to: Alessio Accardi, ala2022@med.cornell.edu

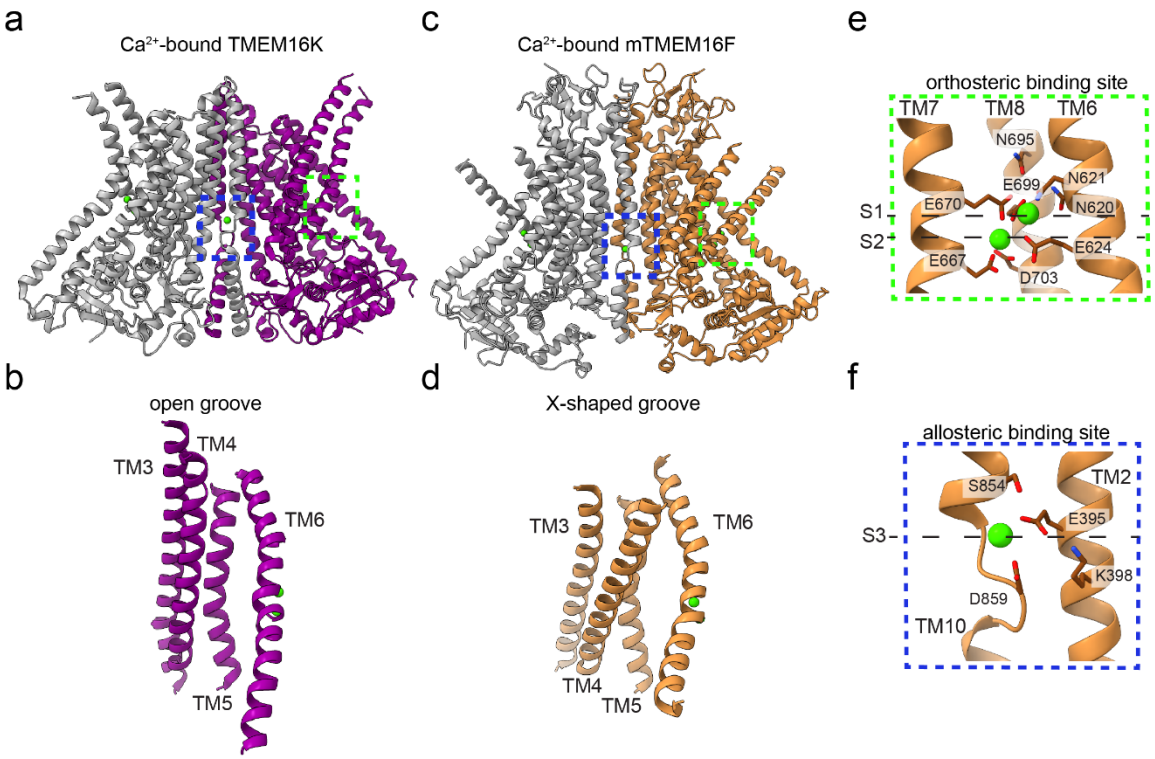

Supplementary Fig. 1: Architecture of TMEM16 proteins. a,c, The structures of Ca^{2+}-bound TMEM16K (**a**) (PDBID: 5OC9) and TMEM16F (PDBID: 9O1N) (**c**) are shown in ribbon representation and viewed from the plane of the membrane. One protomer is colored and the other is shown in gray. Ca^{2+} ions are shown as green spheres. Dashed green or blue boxes indicate the position of the orthosteric and allosteric Ca^{2+} binding sites respectively. **b-d**, Close up view of the groove-lining TM3-TM6 helices in the open conformation of TMEM16K (**b**) and in the X-shaped active state of TMEM16F (**d**). **e,f**, Close up view of the S1 and S2 orthosteric (**e**) and allosteric S3 Ca^{2+} binding sites of TMEM16F (**f**). Side chains coordinating the bound ions are shown in stick representation.

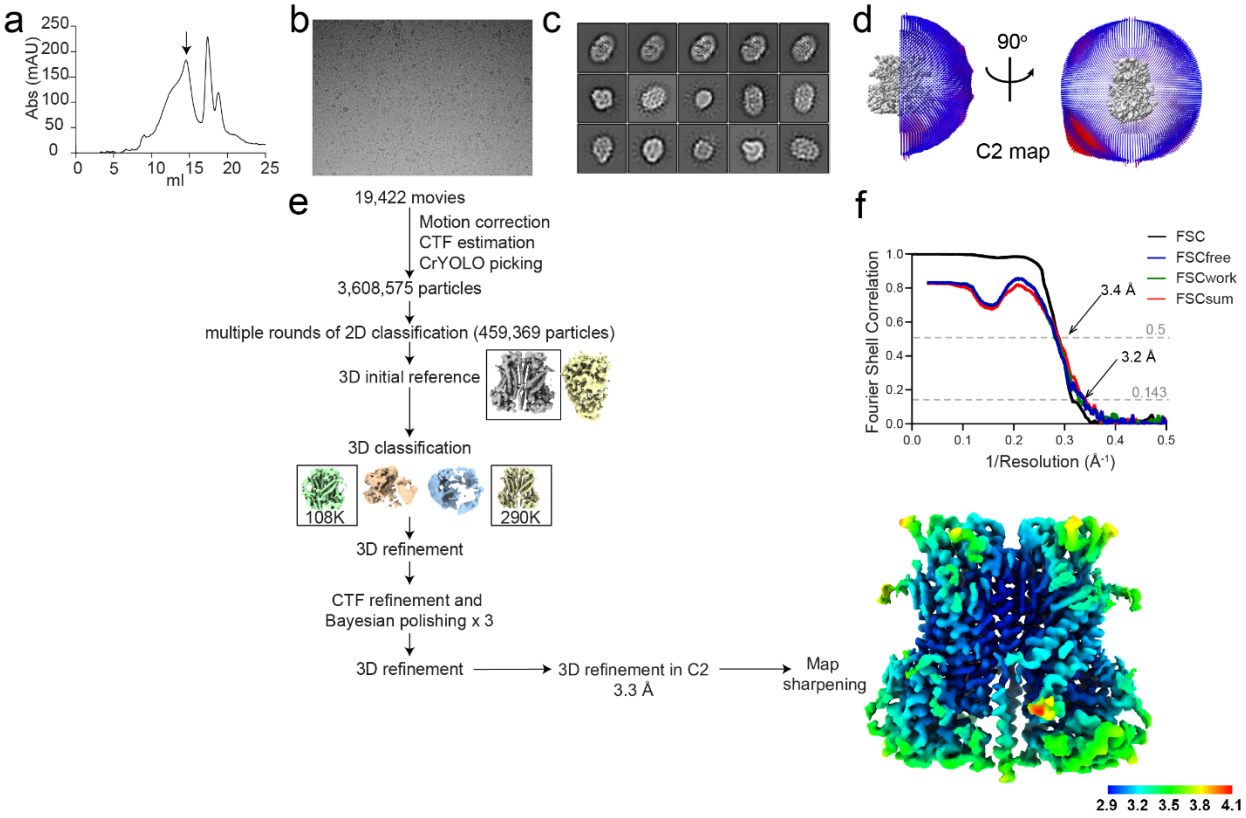

Supplementary Fig. 2, Cryo-EM structure of hTMEM16E in the absence of Ca^{2+}.
a Size exclusion profile of hTMEM16E. Arrow denotes elution position of hTMEM16E. **b** Representative cryo-EM micrograph. **c** Representative 2D classes of hTMEM16E apo. **d** Angular distribution of final C2 reconstruction. **e** Image processing workflow including classification and the final masked reconstruction colored by local resolution calculated using the Relion implementation. **f** FSC plots for dimeric hTMEM16E apo. FSC is between the two half maps to determine the resolution of the reconstruction evaluated at 0.143 cutoff. FSCsum, FSCwork, and FSCfree are model validations evaluated at 0.5 cutoff (see methods).

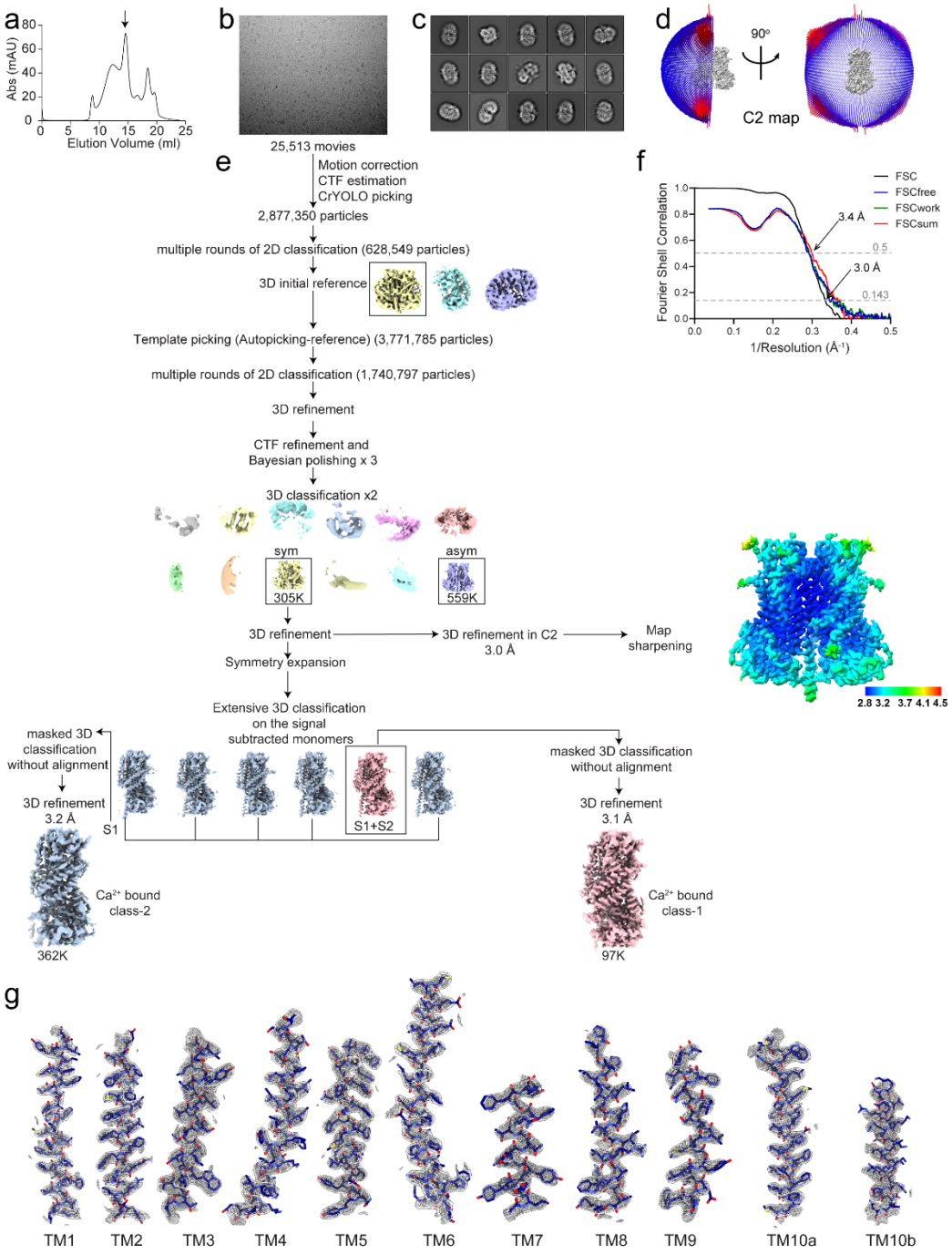

Supplementary Fig. 3, Cryo-EM structure of hTMEM16E in the presence of Ca^{2+}.
a Size exclusion profile of Ca^{2+} bound-hTMEM16E. Arrow denotes elution position of hTMEM16E. **b** Representative cryo-EM micrograph. **c** Representative 2D classes of Ca^{2+} bound-hTMEM16E. **d** Angular distribution of final C2 reconstruction. **e** Image processing workflow including symmetry expansion, classification and the final masked reconstruction colored by local resolution calculated using the RELION implementation. **f** FSC plots for dimeric Ca^{2+} bound-hTMEM16E. FSC is between the two half maps to determine the resolution of the reconstruction evaluated at 0.143 cutoff. FSCsum, FSCwork, and FSCfree are model validations evaluated at 0.5 cutoff (see methods). **g** Cryo-EM densities (contoured at 7.5 σ) superimposed on selected parts of the model.

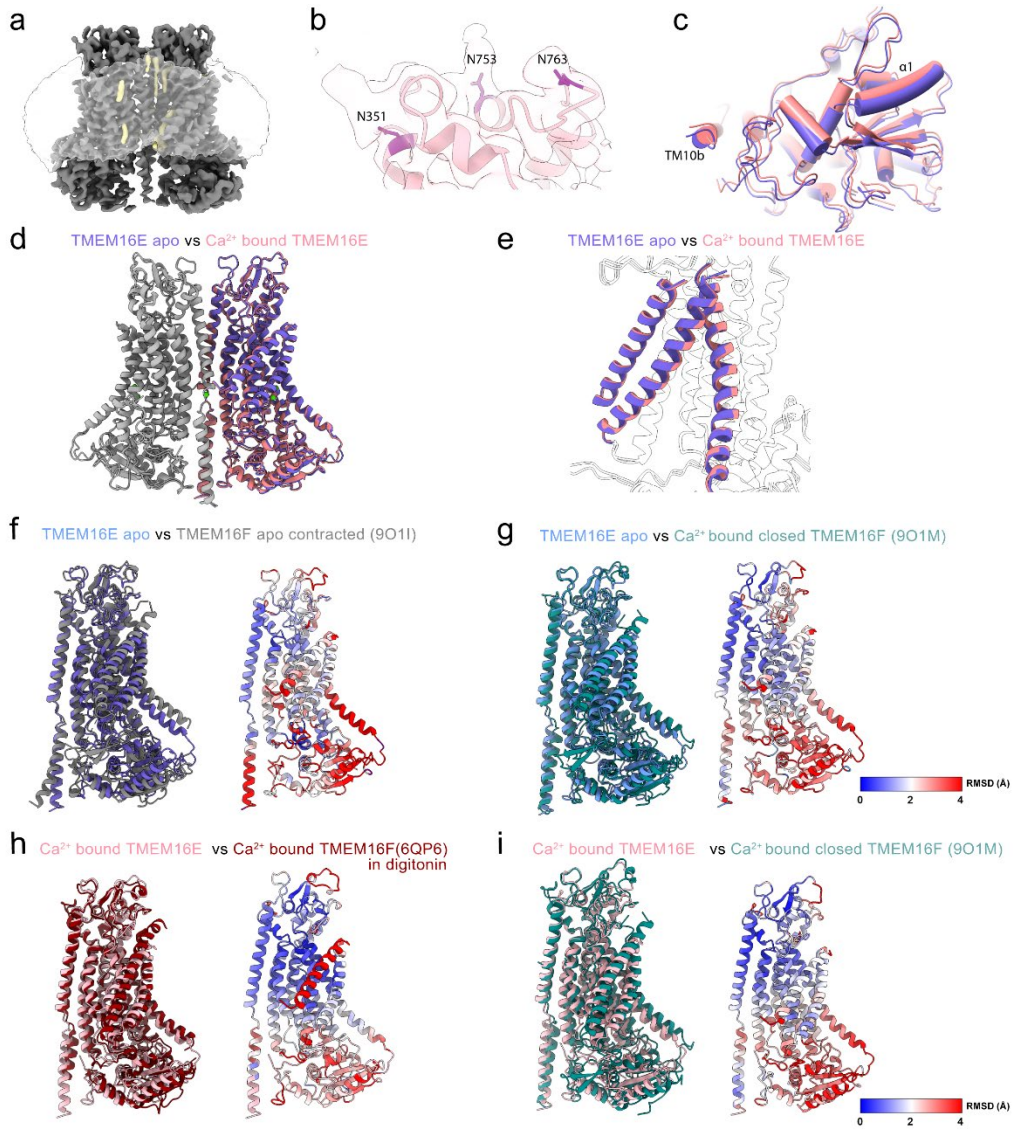

Supplementary Fig.4, Structural characterization of hTMEM16E. a Cryo-EM density map of Ca^{2+}-bound hTMEM16E. The protein density is shown in gray, tubular lipid-like densities are shown in yellow, and the digitonin micelle is shown as a transparent surface. **b** Additional cryo-EM densities observed near putative N-glycosylation sites. The map density is shown as a transparent surface, and the side chains of Asn351, Asn753, and Asn763 are shown as sticks. **c-e** Structural alignments of apo and Ca^{2+}-bound hTMEM16E. Superpositions are shown for the N-terminal cytosolic ferredoxin-like domain (**c**), the full-length protein (**d**), and the membrane-exposed groove region (**e**). Apo hTMEM16E is shown in purple and Ca^{2+}-bound hTMEM16E in salmon. **f-i** Structural comparisons between hTMEM16E and TMEM16F conformations. **f** Apo hTMEM16E, shown in purple, superposed with apo contracted TMEM16F (PDB 9O1I), shown in gray. **g** Apo hTMEM16E, shown in purple, superposed with Ca^{2+}-bound closed TMEM16F (PDB 9O1M), shown in teal. **h** Ca^{2+}-bound hTMEM16E, shown in salmon, superposed with Ca^{2+}-bound TMEM16F in digitonin (PDB 6QP6), shown in dark red. **i** Ca^{2+}-bound hTMEM16E, shown in salmon, superposed with Ca^{2+}-bound closed TMEM16F (PDB 9O1M), shown in teal. In each comparison, the paired panel on the right shows the same alignment with hTMEM16E colored according to per-residue RMS deviation, as indicated by the blue-to-white-to-red scale bars.

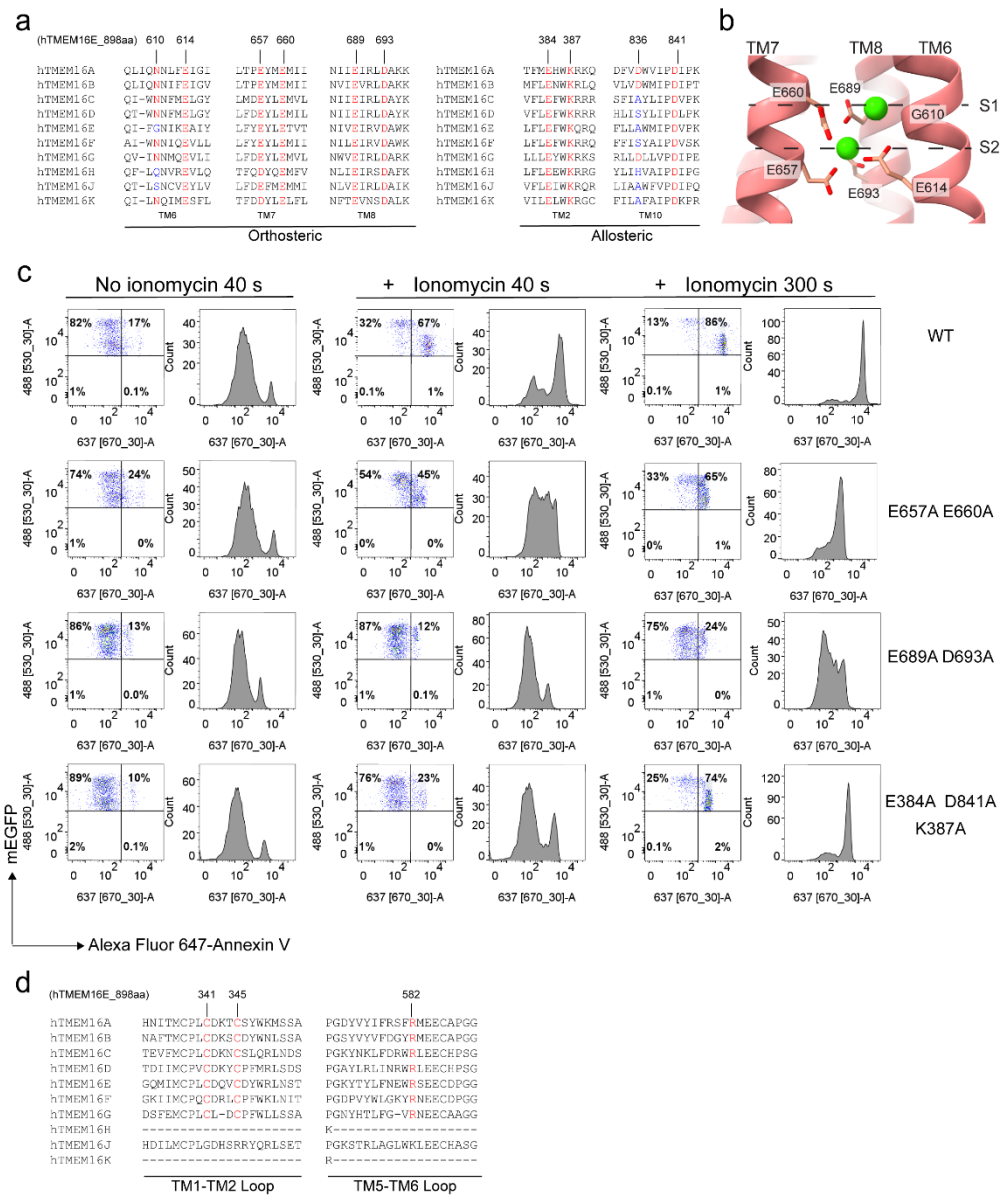

Supplementary Fig. 5: Conservation and function of Ca^{2+} binding residues

a Multiple sequence alignment of human TMEM16 family members at residues contributing to the orthosteric and allosteric Ca^{2+}-binding sites in TM6, TM7, TM8 and TM2, TM10 respectively. Residue numbering refers to the 898-amino-acid hTMEM16E sequence. Conserved residues are highlighted in red, whereas non-conserved residues are highlighted in blue. **b** Close up view of the S1 and S2 orthosteric in hTMEM16E. **c** Flow cytometry analysis of Annexin V staining in cells expressing GFP-tagged wild-type hTMEM16E or Ca^{2+}-binding-site mutants: E657A/E660A, E689A/D693A, and E384A/K387A/D841A. Cells were analyzed in the absence or presence of ionomycin at 40 s and 300 s. DAPI-negative, GFP-positive cells were gated and analyzed for Annexin V signal. For each condition, the left panel shows a two-dimensional scatter plot of Annexin V intensity versus GFP fluorescence, and the right panel shows the corresponding Annexin V intensity histogram. **d** Multiple sequence alignment of human TMEM16 family members showing the conservation of residues C341 and C345 in the TM1–TM2 loop and R582 in the TM5–TM6 loop of hTMEM16E. Residue numbering refers to the 898-amino-acid

hTMEM16E sequence. Conserved residues are highlighted in red.

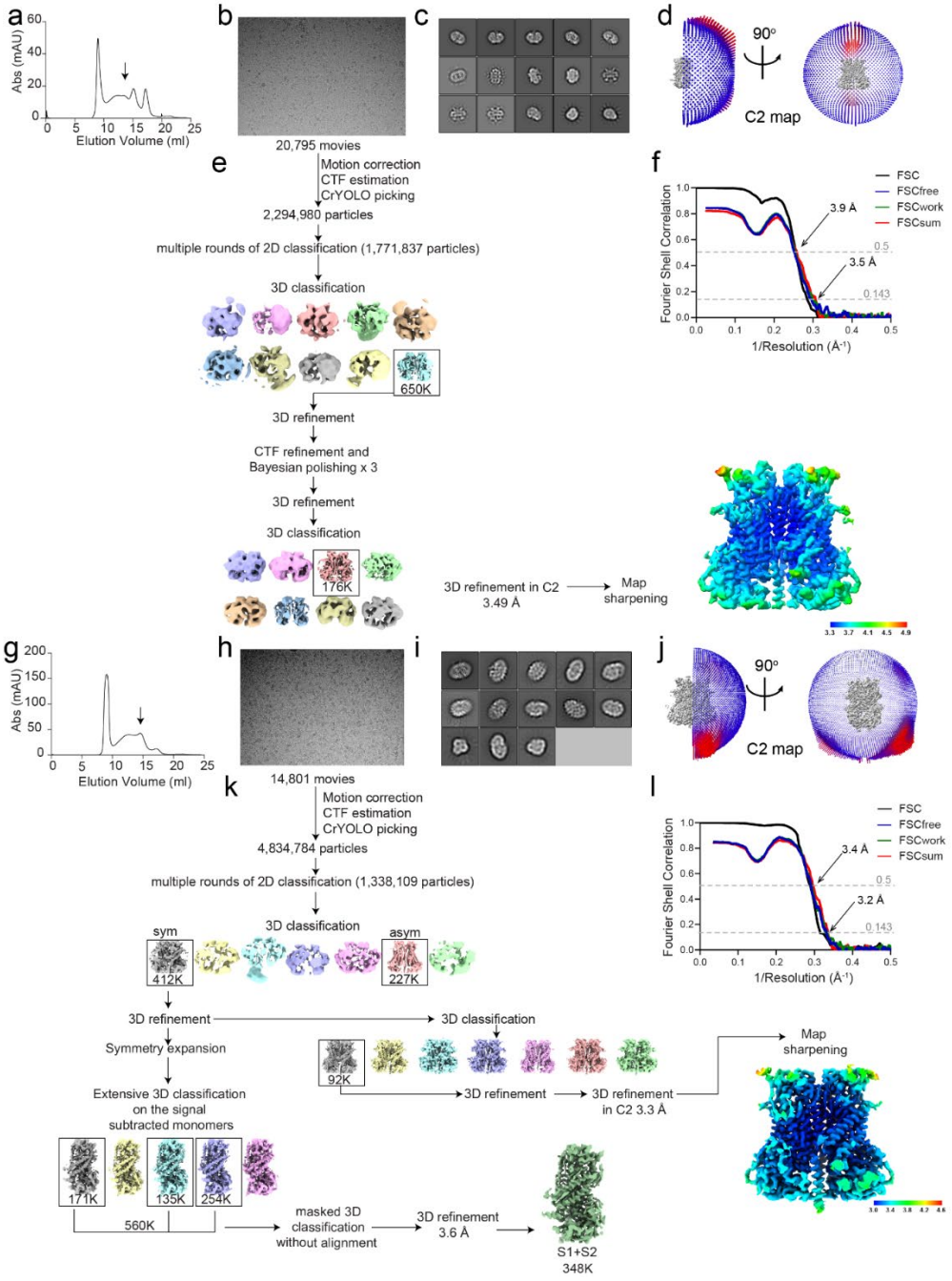

Supplementary Fig. 6: Cryo-EM structure determination of hTMEM16E R582I in the absence and presence of Ca^{2+}. a–l Cryo-EM analysis of hTMEM16E R582I in the absence (**a-f**) or with 1 mM Ca^{2+} (**g–l**). **a, g** Size-exclusion chromatography profiles of purified hTMEM16E R582I in the absence (**a**) or presence (**g**) of Ca^{2+}. **b, h** Representative cryo-EM micrographs. **c, i** Representative 2D class averages. **d, j** Angular distribution plots for the final C2-symmetric reconstructions. **e, k** Image-processing workflows, including the main classification and refinement steps, together with the final sharpened reconstructions colored by local resolution, calculated using RELION. **f, l** Fourier shell correlation curves. Gold-standard FSC curves between independently refined half-maps were used to estimate the global resolutions of the

reconstructions at the 0.143 cutoff. FSCsum, FSCwork, and FSCfree curves were used for model validation and evaluated at the 0.5 cutoff, as described in Methods.

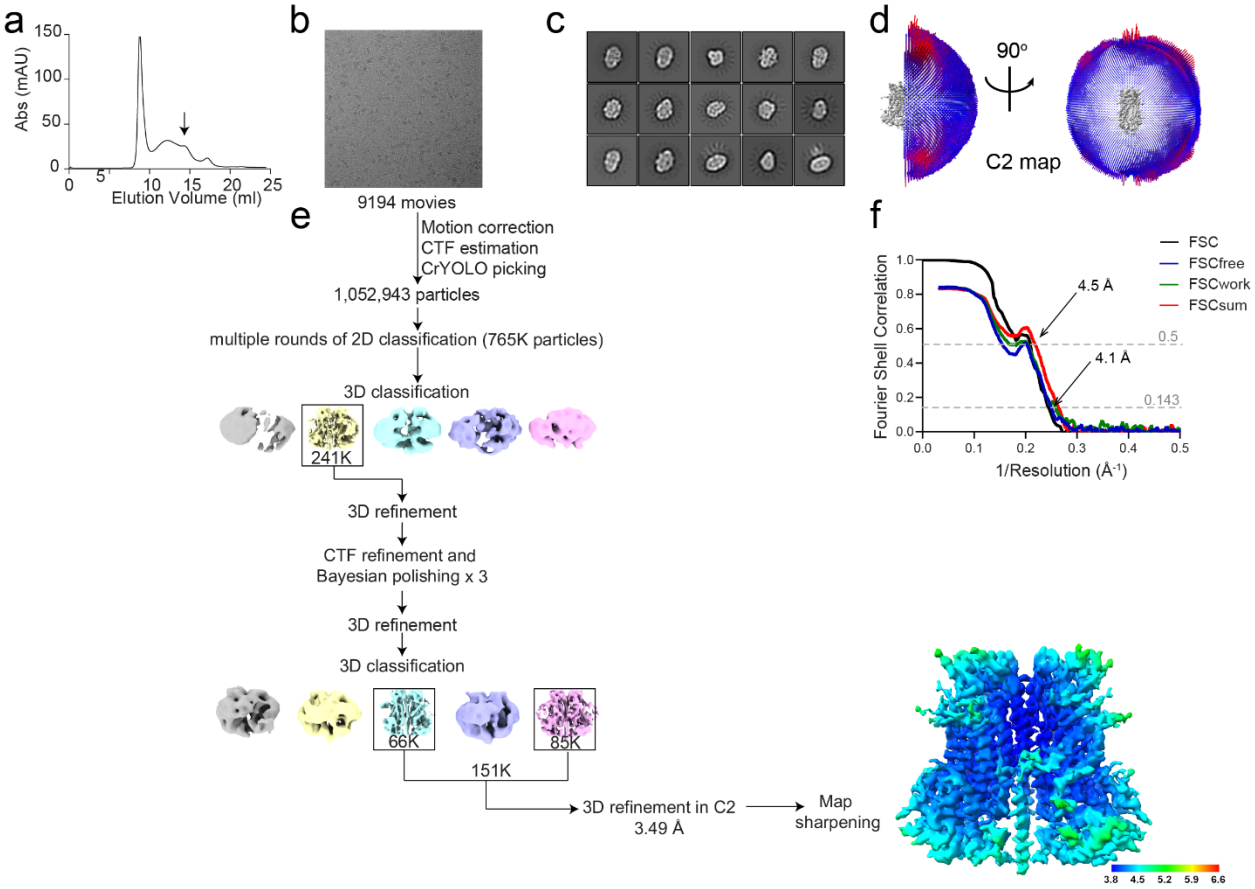

Supplementary Fig. 7: Cryo-EM structure determination of hTMEM16E G503E in the presence of Ca^{2+}.

a Size-exclusion chromatography profile of purified hTMEM16E G503E in the presence of Ca^{2+}. **b** Representative cryo-EM micrograph from the dataset. **c** Representative 2D class averages obtained after multiple rounds of 2D classification. **d** Angular distribution plot of the final C2-symmetric reconstruction. **e** Image-processing workflow and final sharpened reconstruction colored by local resolution, calculated using the RELION implementation. **f** Fourier shell correlation curves for the reconstruction and model validation. The gold-standard FSC between independently refined half-maps was used to estimate the global resolution at the 0.143 cutoff. FSCsum, FSCwork, and FSCfree curves were evaluated at the 0.5 cutoff, as described in Methods.

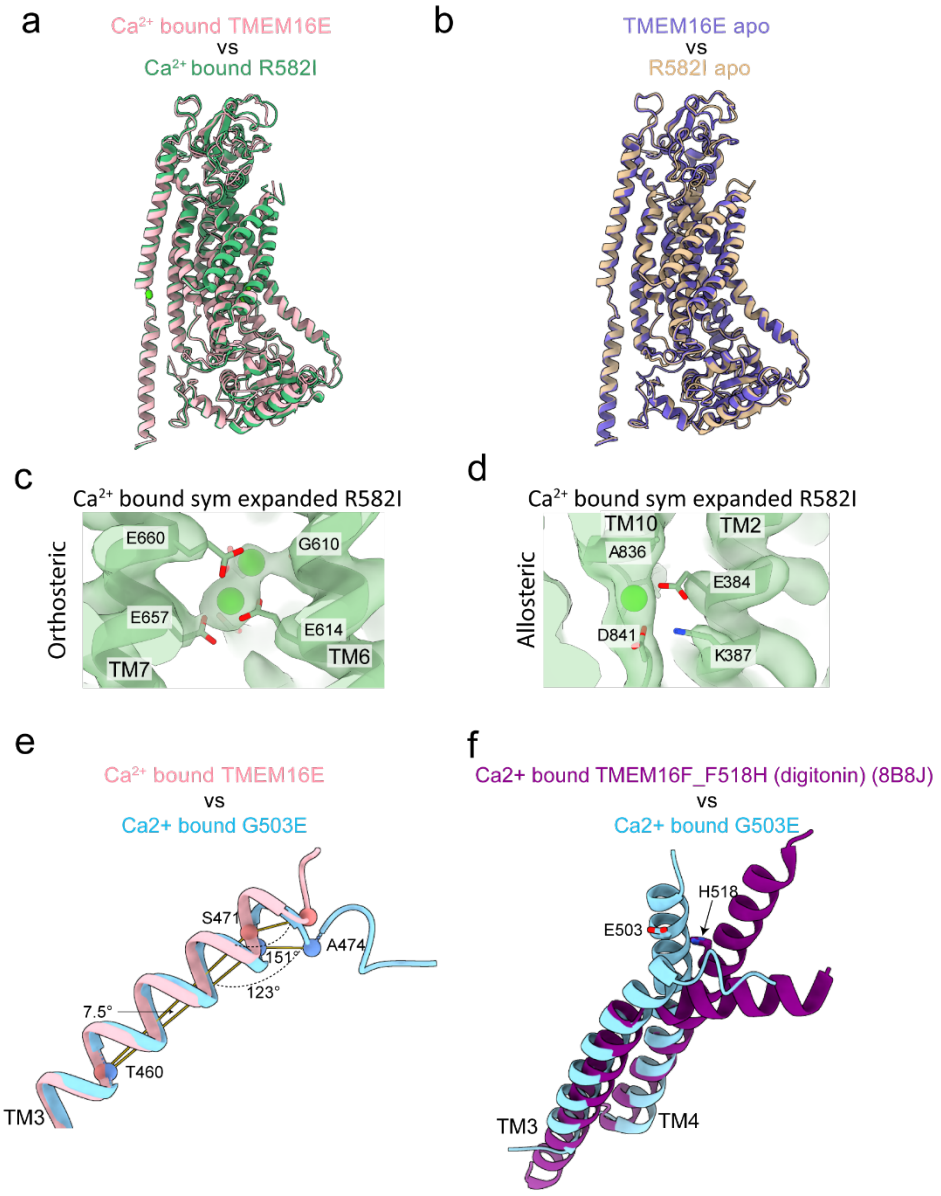

Supplementary Fig. 8: Structural features of hTMEM16E disease-associated mutants.
a, b Structural superpositions of wild-type hTMEM16E and the GDD-associated R582I mutant in the Ca^{2+}-bound **(a)** and apo **(b)** states. Ca^{2+}-bound wild-type hTMEM16E and R582I are shown in salmon and green, respectively; apo wild-type hTMEM16E and apo R582I are shown in purple and beige, respectively. **c, d** Close-up views of the orthosteric **(c)** and allosteric **(d)** Ca^{2+}-binding sites in Ca^{2+}-bound hTMEM16E R582I. Ca^{2+} ions are shown as green spheres, and Ca^{2+}-coordinating residues are shown as sticks. Cryo-EM densities (contoured at 6 σ) superimposed on selected parts of the model. **e** Rearrangement of TM3 induced by the G503E substitution. Superposition of the TM3 region of Ca^{2+}-bound wild-type hTMEM16E and hTMEM16E G503E, shown in salmon and light blue, respectively. The Thr460–Ser471 vector differs by 7.5° between the two models, and the Thr460–Ser471–Ala474 angle decreases from 151° in wild-type hTMEM16E to 123° in hTMEM16E G503E. **f** Superposition of Ca^{2+}-bound hTMEM16E G503E and Ca^{2+}-bound hTMEM16F F518H in digitonin (PDB 8B8J)**,** shown in light blue and magenta, respectively, highlighting the kink of TM3 and displacement of TM4.

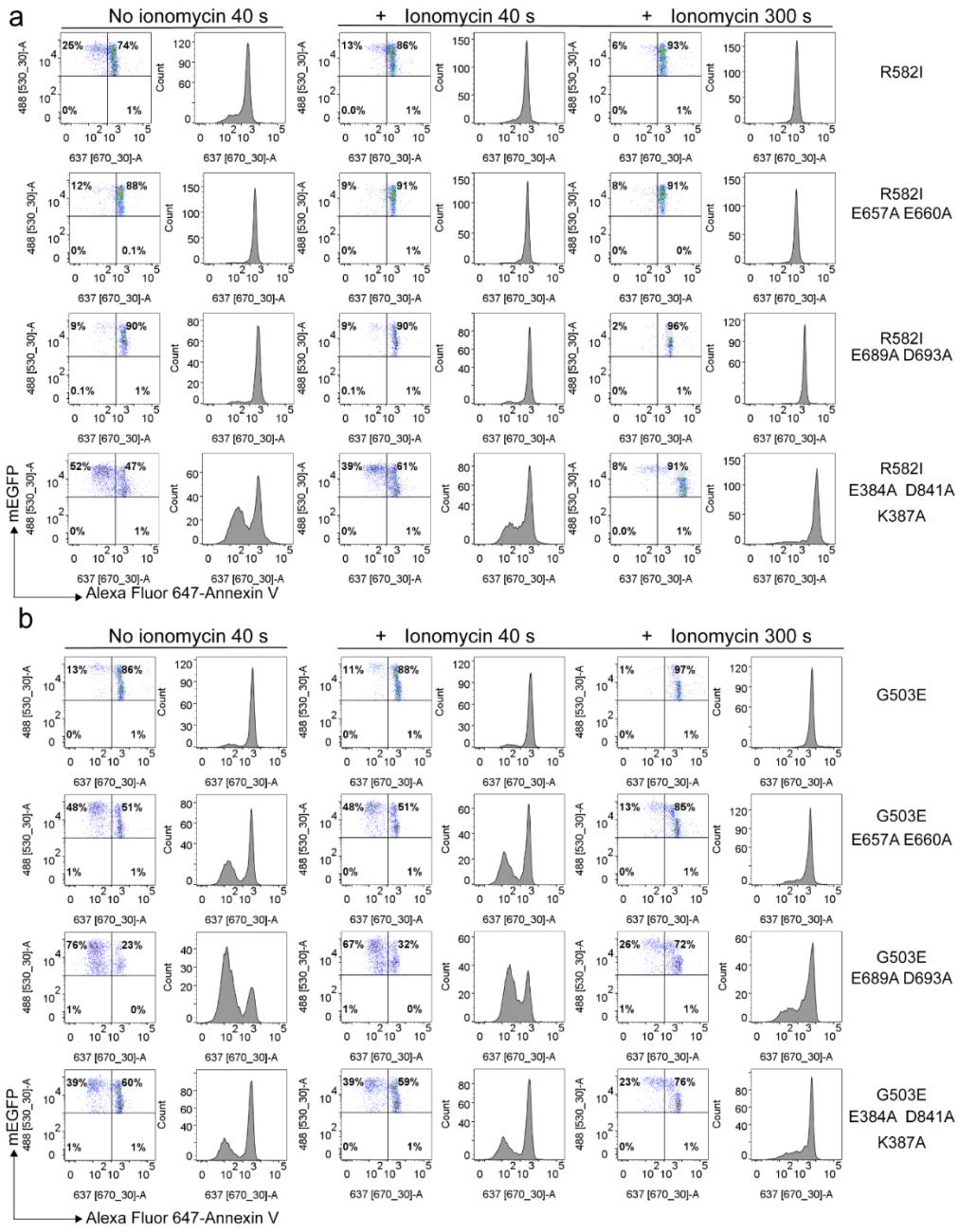

Supplementary Fig. 9: Constitutive activity and Ca^{2+} dependence of hTMEM16E disease-associated mutants.

a, b Flow cytometry analysis of Annexin V staining in cells expressing GFP-tagged hTMEM16E R582I (**a**) or G503E (**b**), either alone or combined with Ca^{2+}-binding-site mutations: E657A/E660A, E689A/D693A, or E384A/K387A/D841A. Cells were analyzed in the absence or presence of ionomycin at 40 s and 300 s. DAPI-negative, GFP-positive cells were gated and analyzed for Annexin V signal. For each condition, the left panel shows a two-dimensional scatter plot of Annexin V intensity versus GFP fluorescence, and the right panel shows the corresponding Annexin V intensity histogram.

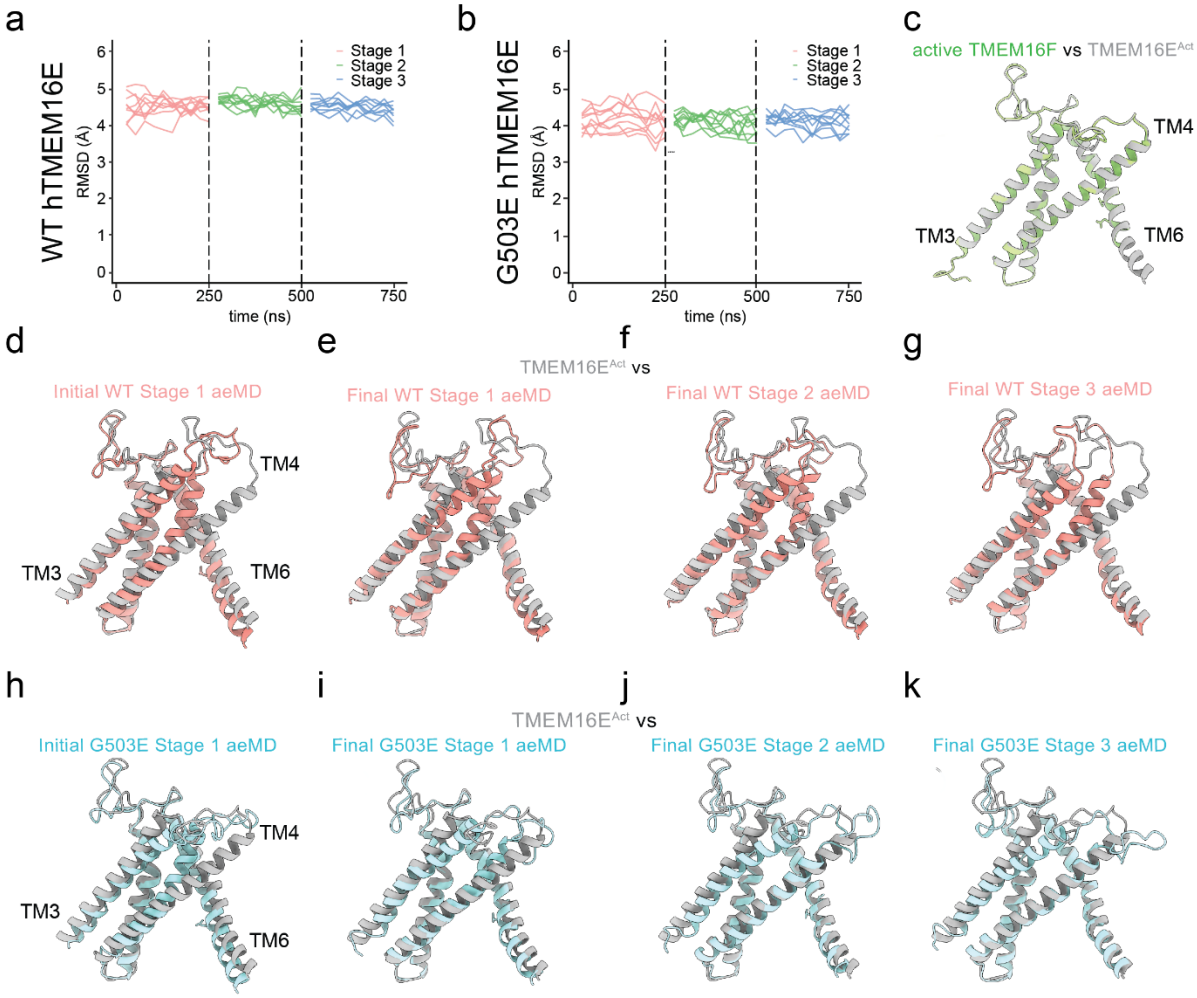

Supplementary Fig. 10: Activation of G503E hTMEM16E. **a,b** Time course of the Cα R.M.S.D. of groove helices TM3-TM6 in protomer B to hTMEM16E^{Act} during adaptive ensemble MD simulation trajectories of WT (**a**) and G503E (**b**) hTMEM16E. Individual traces correspond to each of 10 independent trajectories each 250 ns long. **c** Structural alignment of the groove helices TM3-TM6 of Ca^{2+} bound TMEM16F (PDBID: 9O1N) to the homology model hTMEM16E^{Act}. **d-k** Structural alignment of TM3-TM6 groove helices of hTMEM16E^{Act} to the initial (**d, h**) and snapshots indicated in Fig. 6 (**e-g, i-k**) of the aeMD Stage 1, 2 and 3 trajectories for WT (**d-g**) and G503E (**h-k**) hTMEM16E.